Connecting Scanning Tunneling Spectroscopy to Device Performance for Polymer:Fullerene Organic Solar Cells

Klára Maturová, René A. J. Janssen, and Martijn Kemerink*

Department of Applied Physics, Eindhoven University of Technology, 5600 MB Eindhoven, The Netherlands

ARTICLE

ABSTRACT Scanning tunneling microscopy and spectroscopy have been used to measure the local photovoltaic performance of prototypical polymer:fullerene (MDMO-PPV:PCBM) bulk heterojunction films with ~10 nm resolution. Fullerene-rich clusters are found to act as sinks, extracting electrons from a shell layer of a homogeneously mixed polymer:fullerene matrix, surrounding the fullerene cluster. The experimental results were quantitatively modeled with a drift-diffusion model that in first order accounts for the specific morphology. The same model has subsequently been used to calculate performance indicators of macroscopic solar cells as a function of film composition and characteristic size of the phase separation. As such, a first step has been set toward a quantitative correlation between nanoscopic and macroscopic device photovoltaic performance.

KEYWORDS: organic solar cells · scanning tunneling microscopy · morphology · device modeling

Research on organic bulk heterojunction solar cells has resulted in yearly improvements in their power conversion efficiency that now surpasses ~7% in solar light.[1−4] Evidently, further improvement is greatly helped by a better understanding of the limiting factors of present devices. In particular, it is widely accepted that for polymer:polymer[5,6] and polymer:fullerene[7,8] bulk heterojunction solar cells the degree of crystallinity[9,10] and the separation between the donor and acceptor phases[8−12] are of crucial importance. On the one hand, phase separation in pure acceptor and donor phases promotes crystallization—provided either or both materials are crystalline[13−15]—and promotes the separation of the charge-transfer state at the interface and the collection of free charges. On the other hand, a too strong phase separation reduces the interfacial area between donor and acceptor materials, frustrating the dissociation of excitons into charges. Advanced scanning probe techniques, such as scanning Kelvin probe microscopy (SKPM),[16−20] scanning tunneling microscopy and spectroscopy (STM and STS), and conductive atomic force microscopy (C-AFM),[21] have given valuable information about both the phase-separated morphology and the local electrical properties.[22−24] However, what has been lacking so far is a quantitative link between local photocurrent measurements and a macroscopic device operation.

One of the most well-studied bulk heterojunction solar cell systems consists of the blend of poly[2-methyloxy-5-(3′,7′-dimethyloctyloxy)-*p*-phenylene vinylene] (MDMO-PPV) and 1-(3-methoxycarbonyl)propyl-1-phenyl[6,6]C_{61} (PCBM), which reaches a power conversion efficiency of 2.5% in simulated solar light.[8] At the optimal 1:4 weight ratio, phase separation in MDMO-PPV:PCBM blends occurs into a homogeneous mixed phase, containing roughly equal amounts of MDMO-PPV and PCBM and an almost pure nanocrystalline PCBM phase.[11] In these MDMO-PPV:PCBM blends, the dimension of phase separation and performance of the cells can be adjusted by simply changing the solvent.[8] The best performance is reached using chlorobenzene, resulting in relatively small PCBM clusters. By using toluene, on the other hand, the size of the PCBM cluster increases and the performance deteriorates. Because the type of phase separation in MDMO-PPV:PCBM, and more in particular the role of the size of the PCBM clusters on performance, is to a large extent prototypical for many of the more efficient blends published recently, this blend is an excellent system to correlate nanoscopic properties with macroscopic performance.

Along this line, we recently reported on the surface potential of MDMO-PPV:PCBM blends under illumination and established that an excess of electrons is present in both the mixed phase and the PCBM

*Address correspondence to m.kemerink@tue.nl.

Received for review August 19, 2009 and accepted February 17, 2010.

Published online February 25, 2010. 10.1021/nn100039r

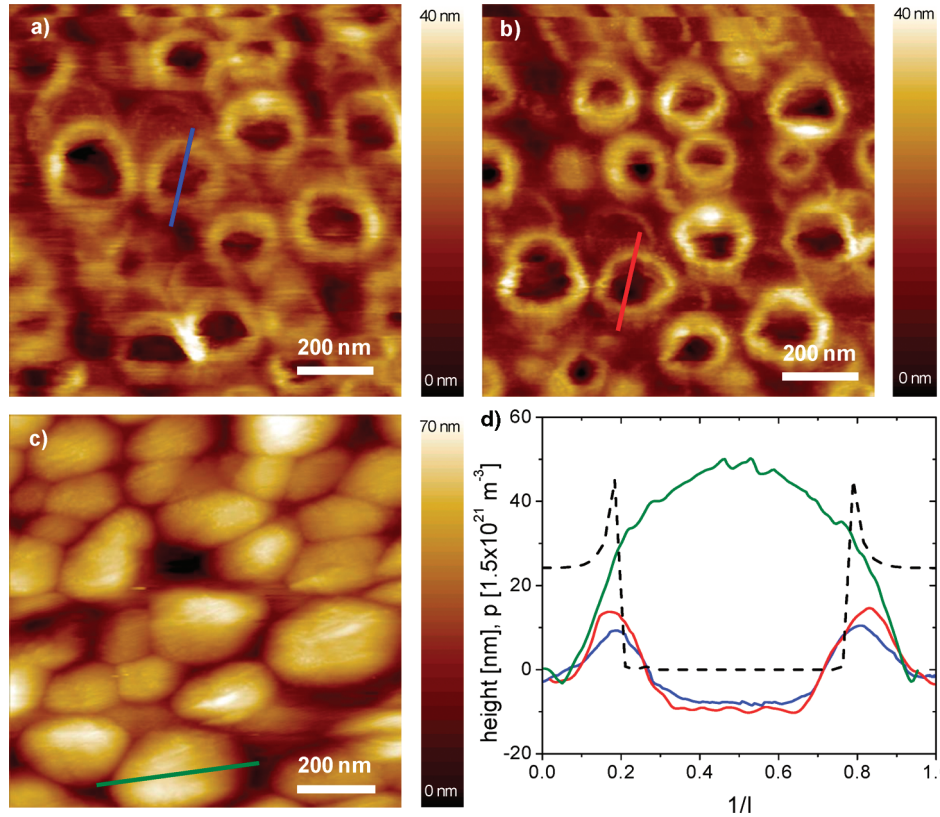

Figure 1. Scanning tunneling microscopy of MDMO-PPV:PCBM thin films spin-cast from toluene: (a) 1 μm × 1 μm topography taken at positive sample bias in the dark; (b) 1 μm × 1 μm topography taken at positive bias under illumination; (c) 1 μm × 1 μm topography taken at negative bias under illumination of the film in (b); (d) cross sections over typical PCBM clusters as probed by STM. Line types correspond to line sections in panels a−c. The dotted black line represents the calculated hole density under illumination across the PCBM cluster. Topographic heights cannot be directly compared as these are taken on different clusters.

clusters.[25] On the basis of these results, we then developed a simple morphological drift-diffusion device model that successfully describes the current voltage (*I*−*V*) characteristics of MDMO-PPV:PCBM cells for different degrees of phase separation.[26] A key feature of this model is that pure PCBM clusters positioned at short lateral distances can act as an effective sink for electrons and reduce the bimolecular recombination of electrons and holes to enhance the performance.

We now present the results of local dark current and photocurrent measurements using scanning tunneling microscopy (STM) and scanning tunneling spectroscopy (STS) on MDMO-PPV:PCBM blends. We find that the current−voltage (*I*−*V*) curves measured at the nanoscopic level are qualitatively and quantitatively explained by the same numerical morphological drift-diffusion model[26] that was used to describe the macroscopic performance of the cells. The model accounts in first order for the lateral phase-separated morphology, and the results clearly support the view that fullerene clusters act as a sink, collecting electrons that were photocreated in the surrounding homogeneous MDMO-PPC:PCBM matrix. With this result, we have been able to make a first step toward directly correlating the performance of nanoscopic and macroscopic solar cells on a quantitative level. Using the same parameters, we performed predictive calculations or macroscopic solar cells of variable composition and morphology that suggest that, for the material system studied, the experimentally realized length scale of lateral phase separation is close to optimal.

RESULTS

Representative images of STM and STS measurements on the MDMO-PPV:PCBM (1:4 w/w) blends are shown in Figure 1. For comparison, AFM and SKPM images and corresponding line sections on the same samples are shown in the Supporting Information, Figures S1 and S2.

STM Topography. STM topographies obtained on films spin-coated from toluene, that is, giving rise to relatively large PCBM clusters, are displayed in Figure 1. Panels a and b of Figure 1 were measured at positive sample bias, in the dark and under illumination, respectively. Figure 1c was measured under illumination at negative sample bias with respect to the virtually grounded tip. Comparison of Figure 1b,c shows that the topographies taken at positive and negative sample bias differ strongly, with the PCBM clusters showing up as protrusions under negative bias, while under positive bias, only the circumference of the clusters can be distinguished clearly. This surprising difference is a di-

rect consequence of the operational principle of STM. The STM feedback loop constantly monitors the tip current and makes adjustments to the tip height to maintain a constant current. To accomplish this, the STM uses a set point, defined by a preset bias and current. If the collected current is low compared to the current set point, the feedback moves the tip forward to enhance the current. For soft, low mobility materials, the point at which measured and preset currents are equal may lie *inside the bulk* rather than *above the surface* of the sample, in which case the tip enters into the layer. The obtained "topographical" images therefore represent a surface of constant conductance in which topographic minima and maxima reflect a reduction and an enhancement of the local conductivity, respectively. This mode of invasive scanning probe microscopy has successfully been used before on organic materials.[27] Surprisingly, we find that tip wear or contamination is relatively unimportant provided suitable scan parameters are used. We therefore stress that despite occasional (uncontrolled) tip changes, showing up as horizontal discontinuities (*e.g.*, in the top part of Figure 1b), all images shown are stable under repeated scanning and reproduce well from sample to sample; see also the Supporting Information Figure S3.

To understand the different images under negative and positive sample bias, it is important to recognize that the polarity of the sample bias determines which charge carrier is probed.[22] At negative sample bias under illumination, the STM topographical image closely resembles the AFM image (Figure S1a). However, the apparent spatial resolution of the STM seems higher, as can be seen from the substructure in the PCBM clusters that is present in STM but which is not observed in AFM. We note that it was impossible to obtain a stable STM topography in the dark at negative sample bias. This indicates that the probed current under illumination is (at least predominantly) a *photo*current and that photocreated *electrons* can be extracted from everywhere on the surface, that is, not only from the PCBM clusters but also from the mixed MDMO-PPV:PCBM phase. The latter observation corroborates the conclusion from our previous work that under illumination excess photogenerated electrons are present in the entire active layer.[25]

At positive set point (Figure 1a,b), we found topographic rings whose diameters correspond to the diameter of PCBM clusters and which resemble the faint bright halo surrounding the PCBM cluster in the SKPM image of Figure S1b. Since electron injection from the high work function tip materials (PtIr, Pt, or Au) is extremely unlikely, the collected current at positive sample bias is attributed to *hole* conduction from sample to tip. Hence, the rings surrounding the PCBM clusters correspond to regions of higher hole conductivity.

In order to confirm this assignment, we used our previously developed morphological drift-diffusion device model (briefly described in the Materials and Methods section) to calculate the hole concentration at the surface of the active MDMO-PPV:PCBM layer under illumination. The model assumes that the PCBM clusters are connected to the top and bottom and not covered by the mixed-phase skin layer. The calculated hole concentration in the topmost layer is shown in Figure 1d as the dotted line. The calculations indeed show an enhanced hole density at the interface of the mixed MDMO-PPV:PCBM and PCBM phases and support our assignment. We stress that this enhanced hole concentration at the interface of the two phases is not a consequence of charge generation that only, or predominantly, would occur at the interface between the acceptor and mixed phases because our device model employs a charge generation rate G that is *constant everywhere* in the mixed MDMO-PPV:PCBM phase and *zero* in the pure PCBM phase. Somewhat fainter rings are also found in dark STM measurements at positive bias, indicating that also in the dark holes diffusing from the bottom contact preferentially localizes at the interface, consistent with the rings observed in the SKPM image.

The very fine phase separation that is known to occur in MDMO-PPV:PCBM (1:4) blends spin-coated from chlorobenzene[8] results in an almost featureless STM topography. As for the toluene-cast film, this finding is consistent with topographies as measured by tapping-mode AFM and by transmission and scanning electron microscopy (see, *e.g.*, refs 8 and 11 and Supporting Information Figure S1c,d).

We conclude this section by noticing that the feedback mechanism on the current makes STM an extremely sensitive probe for local variations in conductivity. However, each topographical image reflects the transport properties only under one particular preset bias. As a complementary technique, we have therefore performed spatially resolved STS measurements, which offer a detailed look at local, nanoscopic, current−voltage relations.

Scanning Tunneling Spectroscopy (STS). During this experiment, both topographical as well as $I-V$ data are simultaneously acquired over the entire scan area. Spectroscopy curves are taken on a square grid; at the moment the scanning tip passes a position at which an $I-V$ curve is to be taken, the scanning is interrupted and the feedback loop disabled while the $I-V$ curve is taken, after which it is re-enabled and scanning continues. The matrix of $I-V$ curves can be depicted as a current map at given bias. Representative $I-V$ curves measured at positive set point bias are given in Figure 2. Significantly different $I-V$ curves are found on different characteristic positions on the sample, that is, on the PCBM clusters, on the mixed phase, and at their interface (Figure 2). Due to the STM feedback system, all $I-V$ curves run through the same (set) point at +2.5 V (7 pA). How-

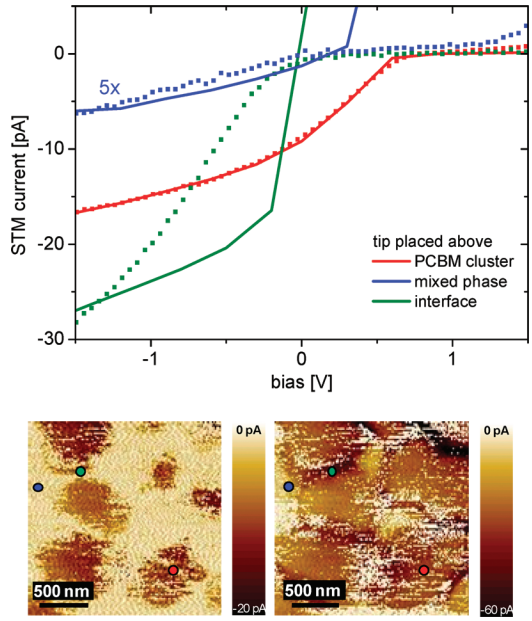

Figure 2. Local *I*−*V* curves under illumination obtained from a STS experiment (colored markers) at positive set point (7 pA, +2.5 V) and from the numerical device model (colored lines) at different positions on the active layer: on the PCBM cluster d_2 = 400 nm (red), on the mixed MDMO-PPV:PCBM phase (blue), and at the interface between the two domains (green). Bottom left and right images show current maps at −2.5 and 0 V, respectively. In the absence of illumination, the current at reverse (negative) bias is zero in both experiment and model.

ever, from a device point of view, the most interesting regime is at reverse bias, on which we shall focus. In the dark, no current could be measured in this regime and, hence, the measured current is entirely carried by photocreated charges. This conclusion is consistent with the impossibility to measure stable STM topographies at negative set point in the dark, as discussed above. By performing similar experiments on pure MDMO-PPV and PCBM, the possibility that the measured photocurrents result from spurious effects as internal photoemission was ruled out; see Supporting Information Figure S4 and accompanying discussion.

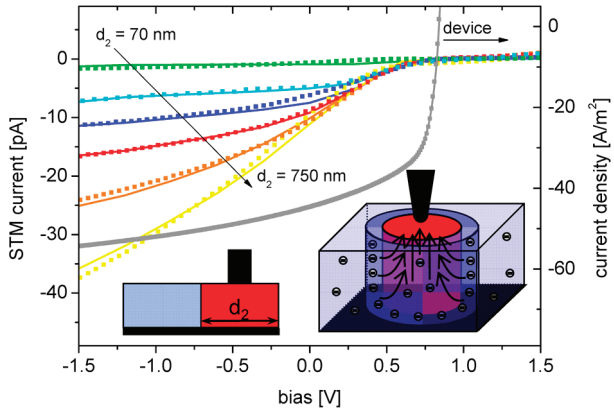

Figure 3. Local *I*−*V* curves for PCBM clusters of different diameter obtained from the numerical model (solid lines: diameter d_2 = 70, 200, 300, 400, 550, 750 nm) and from the STS measurements (symbols: diameter d_2 = 72, 215, 300, 380, 550, 740 nm). Gray symbols and line denote the measured and calculated *I*−*V* curve of the completed bulk device, that is, with a LiF/Al top contact, respectively. The inset illustrates the process responsible for the large photoelectron current extracted from the PCBM clusters.

From the two bulk phases, a much higher current could be extracted at modest reverse bias from the PCBM clusters than from the MDMO-PPV:PCBM mixed phase (*cf.* the blue and red markers in Figure 2). In the case of completed devices, which are typically operated in the same field range, the PCBM clusters, and to a lesser extent the interfacial areas (green markers), will thus facilitate and dominate electron transport to the top contact by acting as electron sinks. For both bulk phases, the behavior at negative bias is relatively well-described by our numerical device model, using exactly the same parameters as used to model the *I*−*V* curve of the bulk device (*cf.* gray line in Figure 3). The highly symmetric geometry assumed in the calculations is realistic for isolated PCBM clusters and "large" areas of mixed material. For the other interfacial areas, this condition is not met and agreement between model and measurement may be expected to be less perfect, as shown by the green line taken on the interface between PCBM and the mixed phase. For bulk device calculations, this symmetry effect is hardly an issue because of the different field distribution with much smaller lateral fields and currents than in STS calculations.

Further insight into the role of the PCBM clusters can be obtained by considering the dependence of the *I*−*V* curve on the cluster diameter. Such curves were collected from several active layers that differed by the degree of phase separation and the size of the PCBM clusters and are plotted along with calculated *I*−*V* curves in Figure 3. The measured local *I*−*V* curves (colored markers) differ substantially in shape from the *I*−*V* curve of the completed device (gray squares), highlighting the need to account for the different geometries used.[28,29] As compared to the macroscopic device, the lower V_{oc} in the STS curves reflects the significantly higher work function of the tip material; the more pronounced field dependence at reverse bias is the result of the different geometry in the STS experiment. More specifically, the STM tip acts as point-like source or sink for currents, injecting or extracting charge into or from a much wider region of the active layer. As a result, averaging local *I*−*V* curves over a large scan area reproduces neither shape nor magnitude of the *I*−*V* curve of a completed bulk device.

The calculated curves in Figure 3 (colored lines) are in good agreement with the measured *I*−*V* curves.[30] We take this as a confirmation that our model gives an accurate description of the role played by the PCBM clusters in the local charge transport. This strengthens the basis of our previous work, in which both the morphology dependence of the device performance and the particular shape of the *I*−*V* curves at intermediate bias were interpreted in terms of electron transport from the mixed phase to the PCBM clusters.[26]

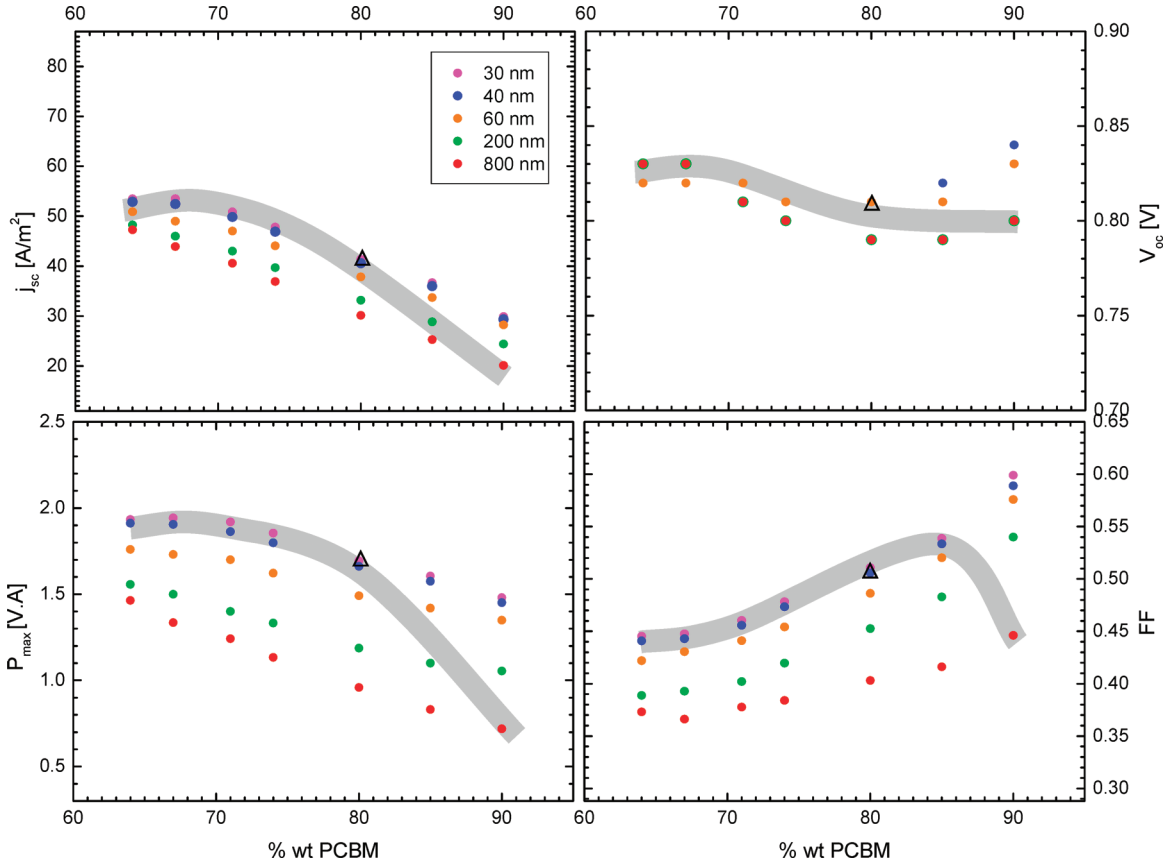

Figure 4. Graphs of device performance: short circuit current density, j_{sc}, open circuit voltage, V_{oc}, maximum electrical output power, P_{max}, and fill factor, FF, for different composition (wt % PCBM) and total lateral width ($d_1 + d_2$ = 30, 40, 60, 200, and 800 nm, as indicated in the legend). Colored circles show calculated values from the device model. The gray band connects calculated points having a morphology that corresponds to the one measured in ref 11; see text for further discussion. Empty triangle: experimental value for the sample shown in Figure 3, *i.e.*, a 20:80 blend of MDMO-PPV:PCBM.

Relation to Morphology. In this last part, we use the numerical device model to make some comments about the relation between composition, morphology, and (bulk) device performance for the MDMO-PPV:PCBM system. In Figure 4, we have calculated the most relevant performance indicators of the solar cell (short circuit current density, j_{sc}, open circuit voltage, V_{oc}, fill factor, FF, and maximum electrical output power, P_{max}) as a function of composition. We have focused on phase-separated samples, having a composition between 60 and 90 wt % of PCBM, for which morphologies ranging from very fine ($d_1 + d_2$ = 30 nm) to very coarse ($d_1 + d_2$ = 800 nm) are considered. The morphology in the 2D model is defined by the sample composition (MDMO:PPV:PCBM ratio) and the typical width $d_1 + d_2$, with d_1 and d_2 the widths of adjacent (2D) slabs of the mixed phase and the pure PCBM phase, respectively. By fixing the composition of the homogeneous mixed phase as 1:1 (wt %, see ref 11), the values of d_1 and d_2 follow from these two parameters. The hole and electron mobilities in the PCBM cluster are taken as 5×10^{-11} and 2×10^{-7} m^2/(V · s), respectively. In the mixed phase, both are chosen in such a way[31] that the effective mobility matches with the data in ref 32. Following this procedure turns the mobility into a given, as opposed to a free, parameter. Table 1 shows typical parameters for the 80 wt % PCBM sample.[26]

Let us now return to the results shown in Figure 4. The decrease in j_{sc} with wt % PCBM is caused by the decreasing amount of absorbing material. On the other hand, the fill factor defined as the ratio of the power in

TABLE 1. List of Parameters Used in the Model (20:80 MDMO-PPV:PCBM)[a]

parameter	value
geometry:	
layer thickness [nm]	100
$d_1 + d_2$ [nm]	30−800
ratio matrix:PCBM slab width	3:7
mobilities:	
$\mu_h$matrix [m^2/(V · s)]	1.40×10^{-8}
$\mu_e$matrix [m^2/(V · s)]	2.00×10^{-10}
μ_hPCBM cluster [m^2/(V · s)]	5.00×10^{-11}
μ_ePCBM cluster [m^2/(V · s)]	2.00×10^{-7}
general parameters	
PEDOT:PSS work function	5.2 eV
tip work function	4.8 eV
LUMO, HOMO of PCBM	4.1 eV, 6.1 eV
LUMO, HOMO of mixed phase	4.1 eV, 5.2 eV

[a]Charge carrier mobilities were taken from ref 32. Parameters for other compositions are calculated as outlined in the text.

the maximum power point and the product of j_{sc} and V_{oc} increases with increasing amount of PCBM due to the improved electron and hole transport with higher PCBM loadings. The open circuit voltage, V_{oc}, is largely independent of composition in the 2D model; the weak compositional dependence is the result of carrier diffusion from the contacts, giving rise to band bending as discussed before.[25] Being the product of these three parameters, the maximal electrical output power $P_{max} = FF \times j_{sc} \times V_{oc}$ reaches a broad maximum around 70 wt % PCBM. To facilitate comparison with experiment, the thick gray line indicates the model predictions for devices with cluster sizes as measured experimentally by van Duren *et al.*[11] for the different compositions. At increasing PCBM concentrations, the size of the PCBM domains, d_2, grows and the gray line moves to points corresponding to larger values for $d_1 + d_2$. The resulting trends in Figure 4 are in good agreement with the experimental results of ref 11; the absolute numbers of j_{sc} and P_{max} being somewhat higher in the present work, as indicated by the triangle at 80 wt % PCBM.

From the data in Figure 4, it is clear that a relatively fine phase separation (magenta, blue, orange circles) gives better device performance than a relatively coarse phase separation (green and red circles), in agreement with earlier observations.[8,11] However, a further reduction in length scale of phase separation (*cf.* blue and magenta circles) does not bring significant improvement in performance. Consequently, these results suggest that further optimization of the longest length scale of phase separation (*i.e.*, $d_1 + d_2$) in this material system alone is unlikely to yield a significant improvement in performance. Evidently, improvements in the molecular scale morphology that lead to, for example, higher carrier mobilities, more efficient charge generation, or an extended absorption spectrum can lead to substantial improvements.

CONCLUSIONS

We have shown that a geometry where the top electrode of the active layer is replaced by a metallic STM tip can be used to extract otherwise inaccessible information on charge transport on a truly local, nanoscopic scale. Depending on whether the topography was monitored at positive or negative bias, photogenerated holes or electrons are probed, respectively. Next, STS has been used to locally measure $I-V$ curves on different characteristic positions in the phase-separated morphology. The $I-V$ curves of PCBM clusters of different size have been calculated using a morphological drift-diffusion device model. We have found that indeed PCBM clusters act as electron sinks, extracting photocreated electrons from the mixed phase. Finally, the numerical device model has been used to evaluate the main performance indicators, such as short circuit current, open circuit voltage, fill factor, and maximum electrical output power *versus* composition and morphology. The results quantitatively relate the photovoltaic performance of bulk heterojunction blends on a nanoscopic level to the macroscopic device performance and highlight the importance of nanoscale transport of photocreated charge carriers in these devices.

MATERIALS AND METHODS

Experimental. The active layers addressed in this study are bulk heterojunctions consisting of a 1:4 w/w blend of MDMO-PPV and PCBM spin-coated in air in UV-filtered dim ambient light from either chlorobenzene or toluene (both 3 mg/mL of MDMO-PPV). Substrates consisted of a 60 nm thick layer of poly(3,4-ethylenedioxythiophene):poly(styrenesulfonate) (PEDOT:PSS, HC Starck electronic grade Baytron PVP AI4083) on clean ITO/glass. All samples were transferred immediately after preparation into a N_2-filled glovebox ($[H_2O] < 1$ ppm, $[O_2] < 1$ ppm, and $T = 20$ °C), where all STM/S measurements were performed. The STM/STS setup consists of a Veeco Multimode AFM/STM controlled by an SPM100 from RHK. A white halogen lamp (~0.4 kW/m^2) was used for illumination during local photocurrent measurements. We used cut PtIr and etched Pt and Au tips but did not observe any relevant differences between the various tips. When switching between light and dark, the tip was always retracted and allowed to thermally equilibrate before the system was re-engaged.

Numerical Model. The numerical model used to interpret the data has been described in detail before.[25,26] In brief, it is based on the coupled drift diffusion, Poisson, and current continuity equations. It accounts for the lateral components of the phase-separated morphology (*i.e.*, possible vertical composition variations are ignored)[33,34] and does so in first order (*i.e.*, only the largest length scale of the full 3D phase-separated morphology is accounted for and mapped onto a 2D structure of alternating slabs). As such, only length scales that are large compared to single molecules or monomers are modeled; by treating mobilities and generation and recombination rates as effective parameters, the obvious fact that they are affected by the molecular scale morphology is implicitly incorporated. Further, in order to keep the number of free parameters minimal, field- and density-independent mobilities, which differ in each phase, are assumed. The morphology is assumed to be a laterally phase-separated layer, consisting of an intimately mixed polymer:fullerene phase next to a pure fullerene phase.[11] Exciton dissociation is assumed to take place exclusively in the bulk of the mixed phase and is taken independent of electric field, again to minimize the number of free parameters and to keep the results physically transparent. In all calculations shown here, the same parameters are used as in previous bulk calculations,[26] the only exception being the top contact in case of STS simulations. Since the tip is in physical contact with the active layer,[35] the tip−sample interface is treated in the same manner as macroscopic contacts, that is, by an injection barrier that sets the interface charge density according to a Boltzmann factor. The magnitude of the injection barrier has to be re-adjusted according to the Fermi level of the tip, which is lower than for LiF/Al, which is normally used as top contact. Moreover, rather than covering the entire active layer, the tip contact leaves the rest of the active layer surface free, as illustrated in the inset of Figure 3, and the boundary condition is changed accordingly. Since the contact area (diameter ~20 nm) is much larger than a single molecular site (<1 nm), place-to-place fluctuations are expected to be largely washed out. This expectation is confirmed by the observation that the current density within any given domain (*i.e.*, a PCBM cluster or the bulk of the mixed phase) is largely independent of position, as can be

seen in Figures S1d and S2 (Supporting Information) and the bottom images of Figure 2. Importantly, no additional fitting parameters are used in the STS simulations as compared to the bulk calculations. Hence, the tip contact area diameter was assumed equal to the apex radius and taken the same for all calculations in Figures 2 and 3. For the PCBM clusters, the calculated $I-V$ curves are independent of the contact area. The physical reason is that for all realistic tip radii the contact area is much smaller than the PCBM cluster size. For the interfacial and mixed-phase regions, this condition is not met and some dependency on tip radius is found, hampering a fully quantitative description of the experimental data.

Acknowledgment. The work of K.M. is made possible by a NanoNed grant (NanoNed is the Dutch nanotechnology initiative by the Ministry of Economic Affairs).

Supporting Information Available: Scanning probe microscopy (AFM, SKPM, STM, and photocurrent map) of MDMO-PPV:PCBM thin films and conductive AFM on pure MDMO-PPV and PCBM films. This material is available free of charge *via* the Internet at http://pubs.acs.org.

REFERENCES AND NOTES

1. Park, S. H.; Roy, A; Beaupre, S.; Cho, S.; Coates, N.; Moon, J. S.; Moses, D.; Leclerc, M.; Lee, K.; Heeger, A. J. Bulk Heterojunction Solar Cells with Internal Quantum Efficiency Approaching 100%. *Nat. Photon.* **2009**, *3*, 297–302.
2. Liang, Y.; Feng, D.; Wu, Y.; Tsai, S. T.; Li, G.; Ray, C.; Yu, L. Highly Efficient Solar Cell Polymers Developed *via* Fine-Tuning of Structural and Electronic Properties. *J. Am. Chem. Soc.* **2009**, *131*, 7792–7799.
3. Chen, H.-Y.; Hou, J.; Zhang, S.; Liang, Y.; Yang, G.; Yang, Y.; Yu, L.; Wu, V; Li, G. Polymer Solar Cells with Enhanced Open-Circuit Voltage and Efficiency. *Nat. Photon.* **2009**, *3*, 649–653.
4. Liang, Y.; Xu, Z.; Xia, J.; Tsai, S.-T.; Wu, Y.; Li, G.; Ray, C.; Yu, L. For the Bright Future - Bulk Heterojunction Polymer Solar Cells with Power Conversion Efficiency of 7.4%. *Adv. Mater.* DOI: 10.1002/adma.200903528.
5. Yu, G.; Heeger, A. J. Charge Separation and Photovoltaic Conversion in Polymer Composites with Internal Donor/Acceptor Heterojunctions. *J. Appl. Phys.* **1995**, *78*, 4510–4515.
6. Halls, J. J. M.; Walsh, C. A.; Greenham, N. C.; Marseglia, E. A.; Friend, R. H.; Moratti, S. C.; Holmes, A. B. Efficient Photodiodes from Interpenetrating Polymer Networks. *Nature* **1995**, *376*, 498–500.
7. Yu, G.; Gao, J.; Hummelen, J. C.; Wudl, F.; Heeger, A. J. Polymer Photovoltaic Cells: Enhanced Efficiencies *via* a Network of Internal Donor−Acceptor Heterojunctions. *Science* **1995**, *270*, 1789–1791.
8. Shaheen, S. E.; Brabec, C. J.; Sariciftci, N. S.; Padinger, F.; Fromherz, T.; Hummelen, J. C. 2.5% Efficient Organic Plastic Solar Cells. *Appl. Phys. Lett.* **2001**, *78*, 841–843.
9. Erb, T.; Zhokhavets, U.; Gobsch, G.; Raleva, S.; Stuehn, B.; Schilinsky, P.; Waldauf, C.; Brabec, C. J. Correlation between Structural and Optical Properties of Composite Polymer Fullerene Films for Organic Solar Cells. *Adv. Funct. Mater.* **2005**, *15*, 1193–1196.
10. Yang, X.; Loos, J.; Veenstra, S. C.; Verhees, W. J. H.; Wienk, M. M.; Kroon, J. M.; Michels, M. A. J.; Janssen, R. A. J. Nanoscale Morphology of High Performance Polymer Solar Cells. *Nano Lett.* **2005**, *5*, 579–583.
11. van Duren, J. K. J.; Yang, X.; Loos, J.; Bulle-Lieuwma, C. W. T.; Sieval, A. B.; Hummelen, J. C.; Janssen, R. A. J. Relating the Morphology of Poly(*p*-phenylene vinylene)-Methanofullerene Blends to Solar-Cell Performance. *Adv. Funct. Mater.* **2004**, *14*, 425–434.
12. Peet, J.; Kim, J. Y.; Coates, N. E.; Ma, W. L.; Moses, D.; Heeger, A. J.; Bazan, G. C. Efficiency Enhancement in Low-Bandgap Polymer Solar Cells by Processing with Alkane Dithiols. *Nat. Mater.* **2007**, *6*, 497–500.
13. Li, G.; Shrotriya, V.; Huang, J.; Yao, Y.; Moriarty, T.; Emery, K.; Yang, Y. High-Efficiency Solution Processable Polymer Photovoltaic Cells by Self-Organization of Polymer Blends. *Nat. Mater.* **2005**, *4*, 864–868.
14. Chirvase, D.; Parisi, J.; Hummelen, J. C.; Dyakonov, V. Influence of Nanomorphology on the Photovoltaic Action of Polymer−Fullerene Composites. *Nanotechnology* **2004**, *15*, 1317–1323.
15. Kim, Y.; Choulis, S. A.; Nelson, J.; Bradley, D. D. C.; Cook, S.; Durrant, J. R. Device Annealing Effect in Organic Solar Cells with Blends of Regioregular Poly(3-hexylthiophene) and Soluble Fullerene. *Appl. Phys. Lett.* **2005**, *86*, 0635021/1–0635021/3.
16. Glatzel, T.; Hoppe, H.; Sariciftci, N. S.; Lux-Steiner, M. C.; Komiyama, M. Kelvin Probe Force Microscopy Study of Conjugated Polymer−Fullerene Organic Solar Cells. *Jpn. J. Appl. Phys.* **2005**, *44*, 5370–5373.
17. Hoppe, H.; Glatzel, T.; Niggemann, M.; Hinsch, A.; Lux-Steiner, M. C.; Sariciftci, N. S. Kelvin Probe Force Microscopy Study on Conjugated Polymer−Fullerene Bulk Heterojunction Organic Solar Cells. *Nano Lett.* **2005**, *5*, 269–274.
18. Chiesa, M.; Bürgi, L.; Kim, J. S.; Shikler, R.; Friend, R. H.; Sirringhaus, H. Correlation between Surface Photovoltage and Blend Morphology. *Nano Lett.* **2005**, *5*, 559–563.
19. Hoppe, H.; Glatzel, T.; Niggemann, M.; Schwinger, W.; Schaeffler, F.; Hinsch, A.; Lux-Steiner, M. C.; Sariciftci, N. S. Efficiency Limiting Morphological Factors of MDMO PPV PCBM Plastic Solar Cells. *Thin Solid Films* **2006**, *511−512*, 587–592.
20. Palermo, V.; Ridolfi, G.; Talarico, A. M.; Favaretto, L.; Barbarella, G.; Camaioni, N.; Samori, P. A Kelvin Probe Force Microscopy Study of the Photogeneration of Surface Charges in All-Thiophene Photovoltaic Blends. *Adv. Funct. Mater.* **2007**, *17*, 472–478.
21. Alexeev, A.; Loos, J. Conductive Atomic Force Microscopy (C-AFM) Analysis of Photoactive Layers in Inert Atmosphere. *Org. Electron.* **2008**, *9*, 149–154.
22. Coffey, D. C.; Ginger, D. S. Time-Resolved Electrostatic Force Microscopy of Polymer Solar Cells. *Nat. Mater.* **2006**, *5*, 735–740.
23. Coffey, D. C.; Reid, O. G.; Rodovsky, D. B.; Bartholomew, G. P.; Ginger, D. S. Mapping Local Photocurrents in Polymer−Fullerene Solar Cells with Photoconductive Atomic Force Microscopy. *Nano Lett.* **2007**, *7*, 740–744.
24. Bull, T. A.; Pingree, L. S. C.; Jenekhe, S. A.; Ginger, D. S.; Luscombe, C. K. The Role of Mesoscopic PCBM Crystallites in Solvent Vapor Annealed Copolymer Solar Cells. *ACS Nano* **2009**, *3*, 627–636.
25. Maturova, K.; Kemerink, M.; Wienk, M. M.; Charrier, D. S. H.; Janssen, R. A. J. Scanning Kelvin Probe Microscopy on Bulk Heterojunction Polymer Blends. *Adv. Funct. Mater.* **2009**, *19*, 1379–1386.
26. Maturová, K.; van Bavel, S. S.; Wienk, M. M.; Janssen, R. A. J.; Kemerink, M. Morphological Device Model for Organic Bulk Heterojunction Solar Cells. *Nano Lett.* **2009**, *9*, 3032–3037.
27. Timpanaro, S.; Kemerink, M.; Touwslager, F. J.; De Kok, M. M.; Schrader, S. Morphology and Conductivity of PEDOT/PSS Films Studied by Scanning-Tunneling Microscopy. *Chem. Phys. Lett.* **2004**, *394*, 339–343.
28. Reid, O. G.; Munechika, K.; Ginger, D. S. Space Charge Limited Current Measurements on Conjugated Polymer Films Using Conductive Atomic Force Microscopy. *Nano Lett.* **2008**, *8*, 1602–1609.
29. Kemerink, M.; Alvarado, S. F.; Müller, P.; Koenraad, P. M.; Salemink, H. W. M.; Wolter, J. H.; Janssen, R. A. J. Scanning Tunneling Spectroscopy on Organic Semiconductors: Experiment and Model. *Phys. Rev. B.* **2004**, *70*, 045202/1–045202/13.
30. Since the model is 2D, a conversion to 3D needs to be made when calculating STS currents. For the case of a tip placed on a PCBM cluster as studied here, it is easily derived that this conversion factor is $I_{3D} = \pi S(d_1 + d_2)d_2 \times J_{2D}$ with d_1 and d_2 being the width of the mixed and PCBM-rich phase, respectively, and I_{3D} and J_{2D} the "real"

3D current from the cluster and the calculated current density in the 2D model, respectively. *S* is a factor of order unity that accounts for the uncertainty in the illumination intensity in the *in situ* STS experiments and for tip geometry and is kept constant for all samples.

31. Literature data on these devices are measured on completed, bulk devices; hence the measured mobilities are a spatial average of the mobilities in the separate phases, *i.e.*, $\mu_{e/h}^{eff} = (\mu_{e/h}^{1} d_1 + \mu_{e/h}^{2} d_2)/(d_1 + d_2)$.
32. Mihailetchi, V. D.; Koster, L. J. A.; Blom, P. W. M.; Melzer, C.; de Boer, B.; van Duren, J. K. J.; Janssen, R. A. J. Compositional Dependence of the Performance of Poly(*p*-phenylene vinylene)-Methanofullerene Bulk-Heterojunction Solar Cells. *Adv. Funct. Mater.* **2005**, *15*, 795–801.
33. Hoppe, H.; Niggemann, M.; Winder, C.; Kraut, J.; Hiesgen, R.; Hinsch, A.; Meissner, D.; Sariciftci, N. S. Nanoscale Morphology of Conjugated Polymer−Fullerene Based Bulk Solar Cells. *Adv. Funct. Mater.* **2004**, *14*, 1005–1011.
34. Martens, T.; d' Haen, J.; Munters, T.; Beelen, Z.; Goris, L.; Manca, J.; d' Olieslaeger, M.; Vanderzande, D.; de Schepper, L.; Andriessen, R. Disclosure of the Nanostructure of MDMO-PPV-PCBM Bulk Hetero-Junction Organic Solar Cells by a Combination of SPM and TEM. *Synth. Met.* **2003**, *138*, 243–247.
35. The absence of a significant tunneling gap at positive set point can, apart from the measured topographies, be concluded from the shape of the *I*−*V* curves, which do not bear any signs characteristic of tunneling.